

Picocavity-Controlled Subnanometer-Resolved Single-Molecule Fluorescence Imaging and Mollow Triplets

Siyuan Lyu, Yuan Zhang,* Yao Zhang, Kainan Chang, Guangchao Zheng, and Luxia Wang*

Cite This: *J. Phys. Chem. C* 2022, 126, 11129–11137

Read Online

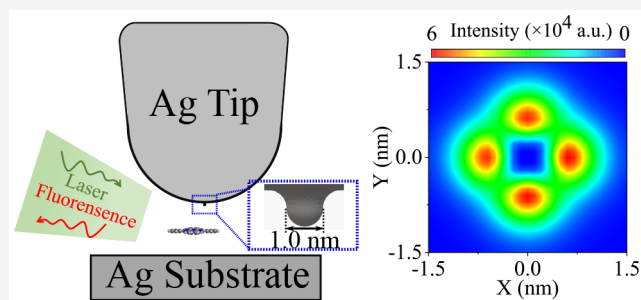
ACCESS |

Metrics & More

Article Recommendations

Supporting Information

ABSTRACT: In this article, we address subnanometer resolved fluorescence imaging of single molecule inside a plasmonic picocavity by proposing a semiclassical theory via combining the macroscopic quantum electrodynamics theory and the open quantum system theory. To gain insights into the experimental results [*Nat. Photonics*, 2020, 14, 694–699, DOI: 10.1038/s41566-020-0677-y], we have further equipped this theory with the classical electromagnetic simulation of the picocavity, formed by atomistic cluster-decorated silver STM tip and a silver substrate, and the time-dependent density functional theory calculation of zinc phthalocyanine molecule. Our simulations not only reproduce the fluorescence spectrum and imaging as measured in the experiment, confirming the influence of extreme field confinement afforded by the picocavity, but also predict Rabi oscillation dynamics and Mollow triplets spectrum for moderate laser excitation. Thus, our study highlights the possibility of coherently manipulating the molecular state and exploring quantum optical phenomena with the plasmonic picocavity.



confirming the influence of extreme field confinement afforded by the picocavity, but also predict Rabi oscillation dynamics and Mollow triplets spectrum for moderate laser excitation. Thus, our study highlights the possibility of coherently manipulating the molecular state and exploring quantum optical phenomena with the plasmonic picocavity.

INTRODUCTION

Recently proposed concept “picocavity” refers to atomistic protrusions inside metallic nanocavities^{1–12} formed by metallic nanoparticle on-film constructs,^{1–4} STM tip on-film structures,^{5–11} or metallic nanoparticle dimers.¹² The atomic protrusions enhance the local field in an atomistic scale due to a nonresonant lightning-rod effect¹² over hundreds fold of enhanced local field afforded by the resonant gap plasmon of the metallic nanocavities. Since the extremely confined field can be smaller than the spatial extension of molecule, its interaction with the typical form of light–matter interaction, which assumes large extension of the electromagnetic field over the molecule, i.e., the dipole approximation. This particular situation requires us to go further and address the influence of the atomistic local field on the light–matter interaction,^{13,14} and on the resulting optical phenomena, such as surface-enhanced Raman scattering^{1–3,5} and surface-enhanced fluorescence.^{8,9,11}

In ref 9, Yang et al. reported experimentally fluorescence imaging with a subnanometer resolution from single zinc phthalocyanine (ZnPc) molecule inside a STM-based metallic picocavity (Figure 1a). In this experiment, a relatively low voltage is applied between the STM tip and the substrate to avoid the tunneled electrons to excite directly the molecule, and the molecule is actually excited by the gap plasmon activated by the laser illumination (see Figure 1c in ref 9), which is completely different from the earlier studies on the molecular electroluminescence.^{15–17} To verify the involvement

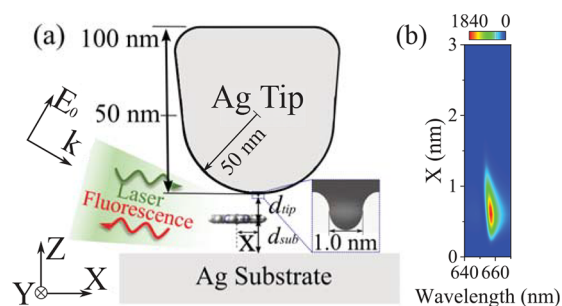
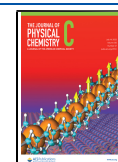


Figure 1. Fluorescence from a single molecule in a picocavity. (a) STM-based picocavity, where the STM tip is modeled as a cone over a hemisphere with size marked and the atomic cluster protrusion is modeled as a sphere of 1 nm diameter (inset), and single zinc phthalocyanine molecule laying horizontally, whose center departs vertically from the substrate by a distance $d_{\text{sub}} = 1.4$ nm (enabled by a NaCl spacer in the experiment), from the STM apex by d_{tip} , and horizontally departs from the apex by X . The picocavity is illuminated by a plane-wave field with amplitude E_0 and wavevector k , which is 30° from the substrate normal, and the fluorescence signal is detected in the reversed path. (b) Calculated fluorescence spectrum according to our theory (for $d_{\text{tip}} = 0.4$ nm).

Received: January 22, 2022

Revised: June 9, 2022

Published: June 28, 2022



of the picocavity, the authors have also studied the influence of the STM tip–molecule distance on the surface-enhanced fluorescence signal, fluorescence line width, and line shift. However, in the corresponding theoretical study, the different quantities are studied with separated formulas, and the internal connection between them is lost.

In the present article, we go beyond the theory developed in ref 9 and propose a semiclassical theory by combining the macroscopic quantum electrodynamics theory^{18,19} and the open quantum system theory.²⁰ Our theory unites different quantities in a coherent manner, and more importantly, it allows us to calculate the fluorescence spectrum, as measured directly in the experiment, which thus provides more insights into the involved physics. Furthermore, we equip our theory with the classical electromagnetic simulations^{21,22} and the time-dependent density functional theory (TDDFT) calculation to investigate the response of the ZnPc molecule to the laser excitation with varying wavelength and intensity. Our simulations not only reproduce the fluorescence spectra and mappings as measured in the experiment (see Figure 1b for an example) but also predict the possibility of observing the coherent Rabi oscillation in the excited-state population dynamics and the Mollow side peak spectrum under moderate laser excitation.

Our article is organized as follows. First, we present our semiclassical theory, including the quantum master equation for the molecular dynamics and the formula to compute the fluorescence spectra. Second, we study the plasmonic response of the picocavity via classical electromagnetic simulations, and the excitation energy and transition current density of the ZnPc molecule via the TDDFT calculation. Third, we investigate the molecule–local field coupling, the plasmonic Lamb shift, and the Purcell-enhanced decay rate, which are then utilized later on to investigate the influence of tip–molecule distance, laser wavelength and laser intensity on the fluorescence spectrum. Finally, we conclude our work and comment on the possible extensions in future.

■ QUANTUM MASTER EQUATION AND FLUORESCENCE SPECTRUM FORMULA

In the section S1 of the Supporting Information, we have considered the interaction between a single molecule and the quantized electromagnetic field of the picocavity according to the macroscopic quantum electrodynamics theory^{18,19} and derived a quantum master equation for the molecule by tracing out the electromagnetic field reservoir. Including the excitation of the molecule and other dissipation processes, we arrive at the following quantum master equation

$$\begin{aligned} \frac{\partial}{\partial t} \hat{\rho} = & -\frac{i}{\hbar} [\hat{H}_m + \hat{H}_{\text{las}}, \hat{\rho}] \\ & + \frac{1}{2} (\Gamma + \gamma) ([\hat{\sigma}^- \hat{\rho}, \hat{\sigma}^\dagger] + [\hat{\sigma}^-, \hat{\rho} \hat{\sigma}^\dagger]) \\ & + \frac{1}{4} \chi ([\hat{\sigma}^z, \hat{\rho} \hat{\sigma}^z] + [\hat{\sigma}^z \hat{\rho}, \hat{\sigma}^z]) \end{aligned} \quad (1)$$

We consider the electronic ground and excited states of the molecule and treat them as two-level system via the Hamiltonian $H_m = \hbar[(\omega_{\text{eg}} + \Omega/2)/2] \hat{\sigma}^z$, where $\omega_{\text{eg}} + \Omega/2$ is the transition frequency (accounting for the plasmonic Lamb shift $\Omega/2$) and $\hat{\sigma}^z$ is the Pauli operator. We treat the optical excitation of the molecule in a semiclassical way and introduce the driving Hamiltonian $H_{\text{las}} = \hbar(\nu e^{-i\omega t} \hat{\sigma}^\dagger + \nu^* e^{i\omega t} \hat{\sigma}^-)$,

where $\hat{\sigma}^\dagger$ and $\hat{\sigma}^-$ are the raising and lowering operators, respectively. The coupling coefficient $\hbar\nu = -\frac{ie}{\omega_{\text{eg}}} \int d^3\mathbf{r} \mathbf{j}_{\text{eg}}(\mathbf{r}) \cdot \mathbf{E}_{\text{loc}}(\mathbf{r}, \omega_1)$ is determined by the local electric field $\mathbf{E}_{\text{loc}}(\mathbf{r}, \omega_1)$ at position \mathbf{r} excited by a laser with frequency ω_1 . Here, e is the elementary charge. The transition current density is defined as

$$\mathbf{j}_{\text{eg}}(\mathbf{r}) = -\frac{i\hbar}{2m_e} [\Psi_{\text{e}}^*(\mathbf{r}) \nabla \Psi_{\text{g}}(\mathbf{r}) - \Psi_{\text{g}}^*(\mathbf{r}) \nabla \Psi_{\text{e}}(\mathbf{r})] \quad (2)$$

with the electron mass m_e and wave functions $\Psi_{\text{g}}(\mathbf{r})$ and $\Psi_{\text{e}}(\mathbf{r})$ of the electronic ground and excited states, respectively. Both wave functions can be computed through the TDDFT calculation; see the discussions later on.

The remaining terms in eq 1 describe the dissipation of the molecule. The second line describes the decay from the excited state with the total rate $\Gamma + \gamma$, where the rate Γ is due to the coupling with the picocavity, known as the Purcell-enhanced decay rate. The third line describes the dephasing rate χ of the molecular transition. The transition frequency shift $\Omega/2$ and the Purcell-enhanced decay rate Γ can be computed with

$$\Omega = -\frac{2e^2}{\hbar\epsilon_0 c^2} \int d^3\mathbf{r} \int d^3\mathbf{r}' \mathbf{j}_{\text{eg}}(\mathbf{r}) \cdot \text{Re} \vec{G}(\mathbf{r}, \mathbf{r}'; \omega_{\text{eg}}) \cdot \mathbf{j}_{\text{eg}}^*(\mathbf{r}') \quad (3)$$

$$\Gamma = \frac{2e^2}{\hbar\epsilon_0 c^2} \int d^3\mathbf{r} \int d^3\mathbf{r}' \mathbf{j}_{\text{eg}}(\mathbf{r}) \cdot \text{Im} \vec{G}(\mathbf{r}, \mathbf{r}'; \omega_{\text{eg}}) \cdot \mathbf{j}_{\text{eg}}^*(\mathbf{r}') \quad (4)$$

Here, ϵ_0 and c are the permittivity and the light speed in vacuum, respectively, and $\vec{G}(\mathbf{r}, \mathbf{r}'; \omega)$ is the classical dyadic Green's function. The function $\vec{G}(\mathbf{r}, \mathbf{r}'; \omega)$ and $\mathbf{E}_{\text{loc}}(\mathbf{r}, \omega_1)$ can be computed through classical electromagnetic simulations; see the discussions later on.

The differential power $\frac{dW}{d\Omega}(\omega)$ at the position \mathbf{r}_d of a detector can be computed with the Fourier transformation of the correlation function of the electric field operators $\hat{\mathbf{E}}(\mathbf{r}_d, \tau)$. Relating the electric field operator with the lowering operator $\hat{\sigma}^-(\tau)$ of the molecule through the dyadic Green's function in the Markov approximation, we finally obtain the expression $\frac{dW}{d\Omega}(\omega) \approx K \text{Re} \int_0^\infty d\tau e^{i\omega\tau} \text{tr}\{\hat{\sigma}^-(\tau)\}$, where $\hat{Q}(\tau)$ satisfies the same eq 1 as $\hat{\rho}$ with however the initial condition $\hat{Q}(\tau) = \hat{\rho}_{\text{ss}} \hat{\sigma}^\dagger$. Here, $\hat{\rho}_{\text{ss}}$ is the density operator at steady-state. In the expression for the differential power, the propagation factor is defined as

$$\begin{aligned} K = & \frac{r^2 \omega_{\text{eg}}^2 e^2}{4\pi^2 \epsilon_0 c^3} \int d^3\mathbf{r}'' \int d^3\mathbf{r}' [\vec{G}^*(\mathbf{r}_d, \mathbf{r}''; \omega_{\text{eg}}) \cdot \mathbf{j}_{\text{eg}}(\mathbf{r}'')] \cdot \\ & [\vec{G}(\mathbf{r}_d, \mathbf{r}'; \omega_{\text{eg}}) \cdot \mathbf{j}_{\text{eg}}^*(\mathbf{r}')] \end{aligned} \quad (5)$$

where r is the distance between the molecular center and the detector.

As a comparison, we consider also the corresponding expressions within the dipole approximation. This approximation assumes that the spatial variation of the quantities $\mathbf{E}_{\text{loc}}(\mathbf{r}, \omega_1)$, $\vec{G}(\mathbf{r}, \mathbf{r}'; \omega)$, and $\vec{G}(\mathbf{r}_d, \mathbf{r}'; \omega_{\text{eg}})$, is much larger than that of the molecular transition density $\mathbf{j}_{\text{eg}}(\mathbf{r})$. As a result, in eqs 3–5, we can replace the position arguments \mathbf{r} , \mathbf{r}' , and \mathbf{r}'' by the molecular center position \mathbf{r}_m , the integration $\frac{ie}{\omega_{\text{eg}}} \int d^3\mathbf{r} \mathbf{j}_{\text{eg}}(\mathbf{r})$ by

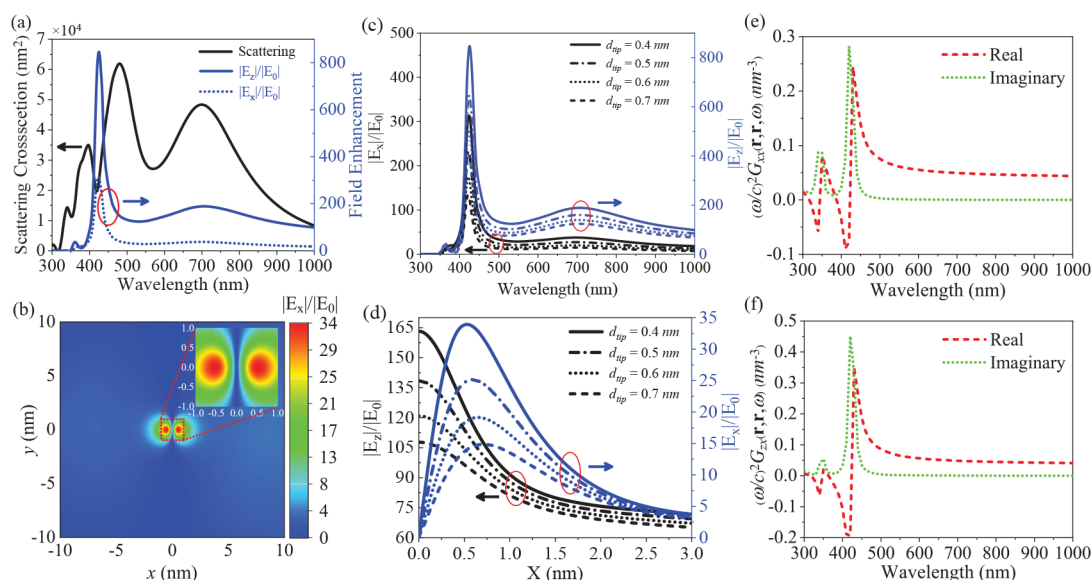


Figure 2. Plasmonic response of the picocavity. (a) Far-field scattering cross section (black solid line, left axis) and the enhancement of local field z - and x -component (blue solid and dashed line, right axis) as a function of wavelength of plane-wave illumination. Here, the z - and x -component are evaluated at the molecular center and a point about 0.5 nm away from the molecular center, respectively. (b) Map of the x -component field enhancement in the middle of the picocavity for the 633 nm plane-wave illumination. (c) Similar results as the near-field component in (a), except that the STM tip-molecule vertical distance d_{tip} varies from 0.4 to 0.7 nm. (d) Field enhancement of the z -component (black lines, left axis) and x -component (blue lines, right axis) as a function of the tip-molecule horizontal distance X for increasing d_{tip} . (e) and (f) Real part (red dashed lines) and the imaginary part (green dotted lines) of the scattered dyadic Green's function for the STM tip about 0.5 nm away from the molecular center.

transition dipole moment \mathbf{d}_{eg} , and dyadic Green's functions by $\vec{G}(\mathbf{r}_m, \mathbf{r}_m; \omega_{\text{eg}})$ and $\vec{G}(\mathbf{r}_d, \mathbf{r}_m; \omega_{\text{eg}})$.

PLASMONIC RESPONSE OF STM-BASED PICOCAVITY

To study the plasmonic response of the STM-based picocavity, as shown in Figure 1a, we carry out the electromagnetic simulations by solving Maxwell's equations with the boundary element method (BEM)^{23,24} as implemented in metallic nanoparticle BEM toolkit,^{21,22} and utilize the permittivity of silver given by Johnson-Christy.²⁵ To mimic the experiment, single ZnPc molecule lays horizontally, and departs from the substrate and the STM apex by a distance $d_{\text{sub}} = 1.4$ nm (enabled by a NaCl spacer in the experiment) and d_{tip} , respectively. As a result, the gap of the STM junction is larger than 1.4 nm, and its response is captured well by the classical electromagnetic simulation within the local response approximation. The nonlocal response and the electron tunneling are normally expected to play a role only for the junction with gap smaller than 1 and 0.5 nm, respectively.^{26,27} Furthermore, we illuminate the plasmonic picocavity with a p-polarized plane-wave field at an incident angle of 30° with respect to the substrate normal (within the x - z incident plane as shown in Figure 1a).

Figure 2a shows the computed far-field scattering cross section (black solid line, left axis), the near-field enhancement of the z -component at the center of the picocavity (blue solid line, right axis), and of the x -component at a point 0.5 nm away horizontally from the center (blue dashed line, right axis). The scattering spectrum shows four peaks at 700, 480, 390, and 340 nm, while the near-field enhancement spectra show mainly two peaks at 707 and 425 nm. The peaks at 700 and 480 nm can be attributed to the (10) and (20) modes according to the nomenclature proposed in ref 28, and the

other peaks are due to the higher-order plasmonic modes. The maxima of the peaks are about 850 and 190 for the field z -component, and the maximum is however about 3 times smaller for the field x -component.

As a comparison, we have also calculated the spectra for a corresponding nanocavity (without the atomic protrusion, see Figure S1) and found that the scattering spectrum is the same but the near-field enhancement is much smaller and does not show the sharp peak at around 410 nm. This comparison indicates that the atomic protrusion affects mainly the local field but not the far field.¹

To further understand the plasmonic response, we have also computed the near-field map in the middle plane of the picocavity for the 633 nm plane-wave illumination; see Figure 2b. The x -component of the local field is minimal at the center, and maximal at two points about 0.6 nm away from the center along the x -axis. The y -component shows a similar pattern except that the maximum occurs along the y -axis (Figure S2a). Both components concentrate in an area of 5 nm size. As a result, the total field in the x - y plane forms a circle with a radius of 0.6 nm (not shown). The field z -component shows the maximum at the center and is much larger compared to other field components, as well as concentrates in an area of 1 nm size over a broad background (Figure S2b).

Since we shall study the change of fluorescence as the STM tip moves away from the molecular center later, we examine here the influence of the vertical distance d_{tip} between the STM tip and the molecule on the local-field enhancement. Figure 2c shows that the field enhancement reduces by about 2 times as the distance d_{tip} increases from 0.4 to 0.7 nm, and the wavelength of the plasmonic resonance blue-shifts slightly. In this range of distances, the molecule does not form a chemical bond with the STM tip, as verified by Figure 3b in the experiment,⁹ and it is beyond the range of the spilled-out

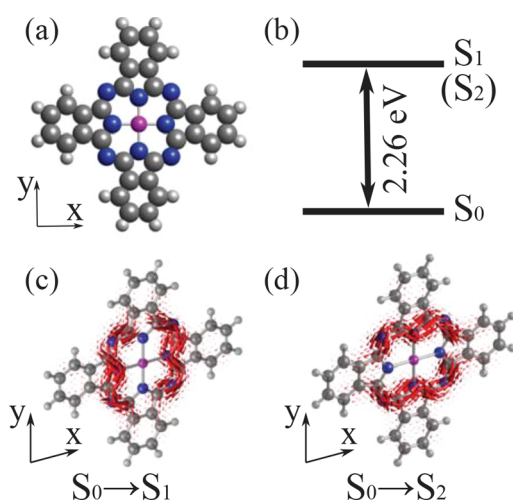


Figure 3. TDDFT calculations of the ZnPc molecule. (a) Atomic structure of the molecule, where white, gray, blue, and pink spheres represent hydrogen, carbon, nitrogen, and zinc atoms, respectively. (b) Energy level diagram with two degenerate excited states. (c) and (d) Transition currents of the two excitonic transitions with vectors around the molecular bonds.

electron (0.3–0.4 nm),²⁹ which again justifies the classical electromagnetic simulations as assumed in the current study. Furthermore, Figure 2d shows that along with the reduced enhancement, the spatial extension of the field component becomes also slightly broadened. Here, we focus on the field x -component and obtain the similar result for the field y -component, and they will affect dominantly the fluorescence, as shown later.

After examining the near-field enhancement, we now study the response of the dyadic Green's function of the picocavity. Figure 2e,f show the real part (red dashed lines) and the imaginary part (green dotted lines) of the xx - and zx -components of the dyadic Green's tensor. The yx -component of the dyadic Green's tensor is very small (Figure S2c) and thus is not shown here. The imaginary part shows two peaks at the same wavelength of maximal field enhancement but does not show a peak around 700 nm. Here, we see also two Fano-features around 420 and 380 nm in the real part (red dashed lines) of the dyadic Green's function. These results indicate that the dyadic Green's function is mainly determined by the gap structure formed by the atomic protrusion and the substrate.³⁰ The prominent feature around 410 nm can be attributed to the Fabry–Perot-like mode of the atomic protrusion as revealed by the electromagnetic simulation within the local response approximation,³¹ and it might be suppressed by the dielectric screening of the tailed electron densities as revealed with the simulation including Landau damping.²⁹ However, our studies of the molecular fluorescence as given below are related to the plasmonic response at longer wavelength around 680 nm, and this response is expected to be only influenced quantitatively by the dielectric screening, as revealed by Figure S1 in ref 29.

TIME-DEPENDENT DENSITY FUNCTIONAL THEORY CALCULATIONS OF ZNPC MOLECULE

In this section, we present the TDDFT calculations of the ZnPc molecule (Figure 3). To obtain these results, we first optimize the structure of the ZnPc molecule (Figure 3a) and then calculate the electronic ground and excited states by using

Gaussian 09 program³² with B3LYP functional and 6-31G(d) basis set. We identify that the transitions HOMO \rightarrow LUMO (LUMO+1) contribute mostly to the $S_0 \rightarrow S_1$ (S_2) excitonic transitions (Figure 3b) with the same excitation energy 2.26 eV, which is larger than the value (1.90 eV) measured in the experiment since TDDFT often overestimates the transition energy. In the following, we will utilize the measured excitation energy in our simulation to ensure the comparison with the experimental results. To calculate the transition current $\mathbf{j}_{\text{eg}}(\mathbf{r})$ according to eq 2, we obtain the wave functions $\Psi_{\text{g}}(\mathbf{r})$, $\Psi_{\text{e}}(\mathbf{r})$ of the HOMO and LUMO (LUMO+1) levels, which are normally given by $\Psi_{\text{g(e)}}(\mathbf{r}) = \sum_i C_i \chi_i(\mathbf{r})$ with the Gaussian-type i th basis function $\chi_i(\mathbf{r})$ and the expansion coefficients C_i , and we calculate the spatial derivative analytically as $\nabla \Psi_{\text{g(e)}}(\mathbf{r}) = \sum_i C_i \nabla \chi_i(\mathbf{r})$. Furthermore, using the relation $\mathbf{d}_{\text{eg}} = \frac{ie}{\omega_{\text{eg}}} \int d^3\mathbf{r} \mathbf{j}_{\text{eg}}(\mathbf{r})$, we also calculate the transition dipole moment \mathbf{d}_{eg} and then verify our calculation by comparing the calculated values with those given in the TDDFT output file.

The calculated transition current $\mathbf{j}_{\text{eg}}(\mathbf{r})$ is presented in our previous article.¹⁴ To gain more insights into $\mathbf{j}_{\text{eg}}(\mathbf{r})$, we show the transition current as vectors around the nitrogen–carbon bonds of the molecule (Figure 3c,d). We find that for the $S_0 \rightarrow S_1$ transition the transition current flows upward along the y -axis, while for the $S_0 \rightarrow S_2$ transition, the transition current flows to the right along the x -axis. Thus, the transition dipole moment, obtained by integrating the transition current over the space, points along the y - and x -axes for the $S_0 \rightarrow S_1$ and $S_0 \rightarrow S_2$ transitions, respectively.

MOLECULE–LOCAL FIELD COUPLING, PLASMONIC LAMB SHIFT, AND PURCELL-ENHANCED DECAY RATE

We can now combine the quantities calculated in previous sections to determine the molecule–picocavity couplings (Figure 4), which include the molecule–local field coupling $\hbar\nu$ for given laser intensity $I_{\text{las}} = 10^2 \mu\text{W}/\mu\text{m}^2$ (black solid line), the plasmonic Lamb shift $\hbar\Omega/2$ (green dashed line), the Purcell-enhanced decay rate $\hbar\Gamma$ (red dotted line), and the propagation factor K (blue dash-dotted line). Here, we focus on the $S_0 \rightarrow S_2$ transition since it dominates the fluorescence under the condition that the STM tip moves along the x -axis, see below. We find that $\hbar\nu$ follows the shape of the near-field enhancement, and it reaches the maximal value around 12 meV at the wavelength of 420 nm. $\hbar\Omega/2$ follows the shape of the real part of the dyadic Green's function, and changes in the range of [−52 meV, 24 meV]. $\hbar\Gamma$ follows the shape of the imaginary part of that function and varies in the range of [0, 160 meV]. For the 652 nm wavelength of the ZnPc excitonic transition, we obtain $\hbar\nu = 1.3$ meV, $\hbar\Omega/2 = -13.9$ meV, and $\hbar\Gamma = 0.25$ meV.

Furthermore, we investigate with Figure 4b how the molecule–local field coupling $\hbar\nu$, the plasmonic Lamb shift $\hbar\Omega/2$, the Purcell-enhanced decay rate $\hbar\Gamma$, and the propagation factor K change with the STM tip–molecule distance X in the horizontal direction. We see that the absolute values of these quantities increase first and then decrease with the increasing distance X . More precisely, the former three quantities reach their maxima around 1.2, −14.3, and 0.25 meV for the distances X around 0.6, 0.39, and 0.6 nm, while the propagation factor reaches the maximum at the distance X around 0.6 nm. As a reference, we have also calculated these parameters by modeling the molecule as a point in the dipole

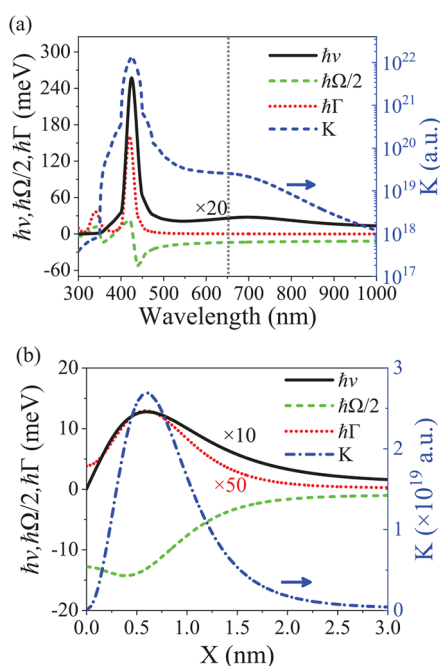


Figure 4. ZnPc molecule–picocavity couplings for the $S_0 \rightarrow S_2$ excitonic transition. (a) Molecule–local field coupling $h\nu$ (black solid line) for the laser power $10^2 \mu\text{W}/\mu\text{m}^2$, the plasmonic Lamb shift $h\Omega/2$ (green dashed line), the Purcell-enhanced decay rate $h\Gamma$ (red dotted line), and the propagation factor K (blue dash-dotted line) as a function of wavelength for the STM tip about 0.5 nm horizontally away from the molecular center, where the vertical black dashed line shows the wavelength of the molecular transition. (b) Change of $h\nu$, $h\Omega/2$, $h\Gamma$, and K as the STM tip moves horizontally away from the molecule along the x -axis for the ZnPc excitonic transition at the wavelength 652 nm.

approximation (see Figure S3) and found similar results except that the values are relatively larger, and the plasmonic Lamb shift and the propagation factor reach the maximum at zero distance. Although the results of the point dipole model and the transition current density model are similar, the slight differences between them indeed lead to some perceived differences in the fluorescence spectrum and mapping, as explained below.

PICOCAVITY-CONTROLLED FLUORESCENCE SPECTRA

We are now in the position to study the picocavity-controlled fluorescence imaging of a single ZnPc molecule. In the following, we first investigate the change of the fluorescence spectrum as the STM tip moves horizontally and vertically and then study the mappings based on the fluorescence intensity, line-shift, and broadening, demonstrating that our calculations can reproduce the experimental results. Then, we go beyond the experiment, and explore the influence of the laser wavelength and intensity on the molecular dynamics and the fluorescence spectrum.

Fluorescence Spectra for Different Tip-Molecule Distances. In their experiment,⁹ Yang et al. had investigated the dependence of the fluorescence spectrum on the STM tip–molecule distance to verify that the subnanometer resolution of fluorescence mapping is afforded by the extremely confined field inside the plasmonic picocavity. Thus, to verify the validity of our theory of the picocavity-controlled fluorescence,

in this section, we also calculate the fluorescence spectrum as the STM tip moves along the x -axis. Here, we focus on the $S_0 \rightarrow S_2$ excitonic transition since this transition dominates the fluorescence, as shown later.

Figure 5a shows that as the tip–molecule horizontal distance X increases from 0 to 3 nm, the fluorescence spectra blue-shift

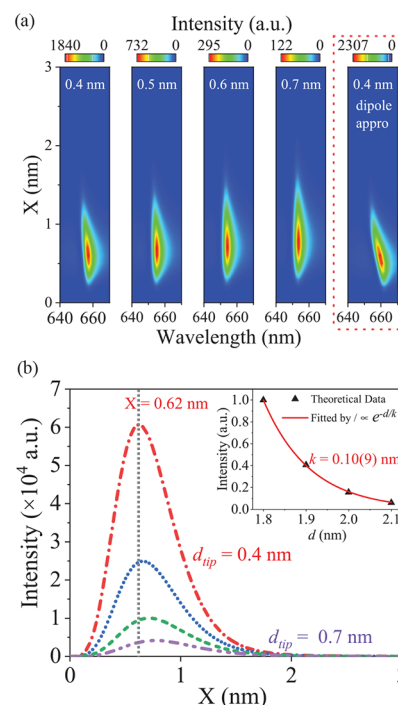


Figure 5. Picocavity-controlled fluorescence of a single ZnPc molecule. (a) Evolution of fluorescence spectra as a function of the tip–molecule horizontal distance X for the increased vertical distance d_{tip} from 0.4 to 0.7 nm (panels 1–4), and the result for $d_{\text{tip}} = 0.4$ nm within the dipole approximation (rightmost panel). (b) Integrated fluorescence signal as a function of X for increasing d_{tip} (from top to bottom curves), and the change of intensity at the distance $X = 0.62$ nm as the gap thickness of the STM junction, normalized by the intensity for the smallest thickness (inset). In all the simulations, we focus on the $S_0 \rightarrow S_2$ excitonic transition with current density along the x -axis, the laser wavelength and intensity are 633 nm and $I_{\text{las}} = 10^2 \mu\text{W}/\mu\text{m}^2$, respectively, and the dephasing rate and the intrinsic decay rate are assumed as $h\chi = 2.3$ meV and $h\gamma = 8.2$ meV.

slightly, and their intensities first increase and then decay to zero, and the horizontal distance for the vanishing spectrum increases with the increasing vertical distance d_{tip} . These results agree qualitatively with Figure 2b in ref 9. As a comparison, we also show the result within the dipole approximation (the rightmost panel of Figure 5a) and find a larger redshift of the spectrum for smaller horizontal distances, which is caused by the overestimated plasmonic Lamb shift within the dipole approximation, as explained in the previous section.

To quantify the influence of the tip–molecule distance, we study the fluorescence intensity I_{flu} integrated over the wavelength range [647 nm, 664 nm] as a function of the tip–molecule horizontal distance X for different tip–molecule vertical distances d_{tip} (Figure 5b). We can see that all the lines first increase and then decrease with increasing X , and the distance to reach the maximum also increases slightly with increasing d_{tip} . Furthermore, we plot the intensity at the distance $X = 0.62$ nm as a function of the gap thickness d of the

STM junction (inset), and fit the result with an exponential function $e^{-d/k}$, leading to the parameter $k = 0.10$ nm. All these results agree qualitatively with Figure 2b,c,d in ref 9.

Mappings with Fluorescence Intensity, Line-Shift, and Broadening. In this section, we turn our attention to the influence of the STM tip–molecule horizontal distance; see Figure 6. To simplify the discussion, we characterize the

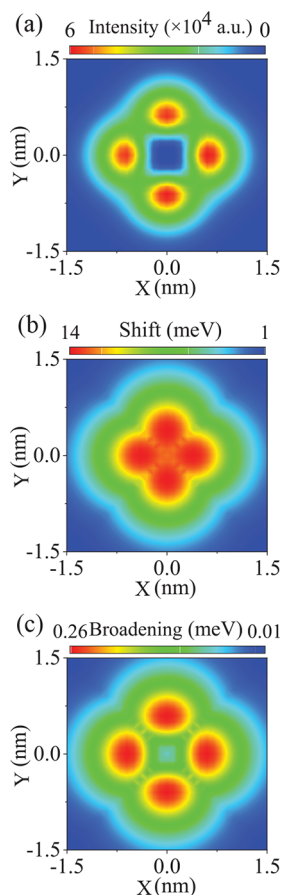


Figure 6. Imaging with fluorescence from single ZnPc molecule in a plasmonic picocavity. (a–c) Imaging based on the fluorescence intensity (a), lineshift (b), and line width broadening (c). To achieve these mappings, the STM tip is $d_{\text{tip}} = 0.4$ nm vertically away from the molecule, and it is moved in the horizontal plane around the molecule. Here, we consider the two transitions $S_0 \rightarrow S_2$ and $S_0 \rightarrow S_1$ with current density along the x - and y -axis. Other parameters are same as in Figure 5.

fluorescence spectrum with the integrated intensity (Figure 6a), line-shift (Figure 6b), and linewidth broadening (Figure 6c), and plot these quantities as a function of the STM tip position in the x – y plane (with the molecule at the origin), leading to 2D mappings. To achieve these results, we have considered the two transitions $S_0 \rightarrow S_2$ and $S_0 \rightarrow S_1$ with the transition current density along the x - and y -axis. All the mappings show maxima for positions about 0.6 nm away from the origin, and relatively small value at the center, forming four lobes. The four-lobe feature agrees qualitatively with Figures 2f and 4c,d of ref 9, verifying again our theoretical model.

To obtain the mapping with the fluorescence intensity, we have calculated the mappings of the molecule–local field couplings ν_{S_1} and ν_{S_2} for the $S_0 \rightarrow S_1$ and $S_0 \rightarrow S_2$ transition, calculated the mappings of the populations P_{S_1} and P_{S_2} for the

two excited states S_1 and S_2 , and finally multiplied them with the propagation factor K_{S_1} and K_{S_2} to obtain the mappings of the fluorescence intensities I_{S_1} and I_{S_2} ; see Figure S6. We find that all the mappings show two lobes along the y - and x -axis for the $S_0 \rightarrow S_1$ and $S_0 \rightarrow S_2$ transition, respectively, which reflects the direction of the current density for these transitions. By comparing these results with Figure 6a, we can attribute the two lobes along the y - and x -axis to the $S_0 \rightarrow S_1$ and $S_0 \rightarrow S_2$ transition, respectively.

To obtain the mapping with the fluorescence line-shift and line width broadening, we calculate first the Lamb shifts $\Omega_{S_1}/2$ and $\Omega_{S_2}/2$ and the Purcell-enhanced decay rates Γ_{S_1} and Γ_{S_2} for the two excited states S_1 and S_2 as a function of the STM tip position. All the mappings show two lobes along the y - and x -axis, respectively. Then, we compare $\Omega_{S_1}/2$, $\Omega_{S_2}/2$ and Γ_{S_1} , Γ_{S_2} of the two transitions and take the large value for given STM tip position, and finally form the mappings shown in Figure 6b,c. Comparing these mappings with the mapping of the fluorescence intensity, we find that the former mappings are more spread, and they do not vanish at the origin. These subtle differences occur since the fluorescence intensity, line-shift, and linewidth broadening are determined by different quantities, namely, the local field enhancement and the real and imaginary part of the dyadic Green's function, respectively. Furthermore, we have also calculated the mappings based on the model within the dipole approximation (not shown) and obtained the similar results as shown in Figure 6 except that the plasmonic Lamb shifts are comparably large at origin, which agrees with the observation from Figure 5.

Fluorescence Spectrum for Different Laser Wavelength and Intensity. So far, most of studies on the picocavity have focused on the subnanometer resolution of the optical imaging afforded by the extreme field confinement.^{2,3,5,8,9,11,33} However, less attention has been paid to the extremely large field enhancement, which accompanies also with the picocavity. Thus, in the following, we explore how the large field enhancement can affect the molecular dynamics and the fluorescence spectrum, see Figure 7.

Figure 7a,b show the dynamics of the excited state population $P_e = (\langle \hat{\sigma}^z \rangle + 1)/2$ and the fluorescence spectrum, respectively, for the 652 nm laser illumination with increasing intensity I_{las} . For $I_{\text{las}} = 10^3 \mu\text{W}/\mu\text{m}^2$, P_e increases first monotonously and then saturates, and the fluorescence spectrum shows a single peak. For larger I_{las} , P_e shows oscillatory behavior before reaching the saturated value, and the fluorescence spectrum shows three peaks. As I_{las} further increases, the period of the oscillations decreases, and the saturated population increases. In the meanwhile, the spectral intensity increases, and the peaks with long and short wavelength redshift and blueshift, respectively. These results indicate that for large I_{las} , the molecule can be coherently excited to the superposition of the electronic ground and excited state, forming the so-called dressed states and leading to the Mollow triplet in the spectrum.^{34,35} In Figure 7c, we summarize the evolution of the saturated P_e (black solid line, left axis) and the integrated fluorescence intensity I_{flu} (blue dotted line, right axis) with increasing laser intensity I_{las} . We see that both P_e and I_{flu} increase linearly for small I_{las} , then sublinearly increase for moderate I_{las} , and finally saturate for larger I_{las} .

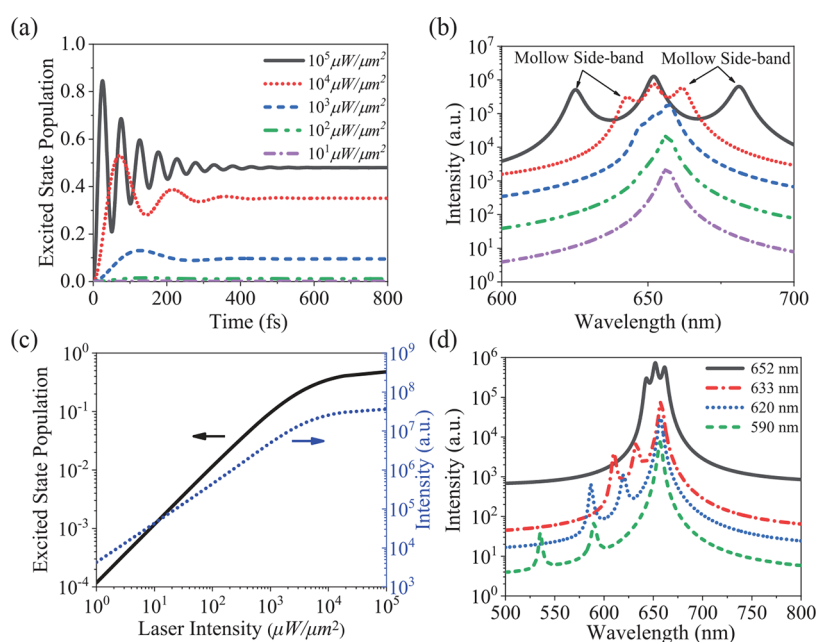


Figure 7. Molecular dynamics and fluorescence. (a) and (b) Dynamics of the excited state population and the fluorescence spectra of single ZnPc molecule, respectively, for the resonant CW laser excitation with wavelength $\lambda_{\text{las}} = 652$ nm and increasing intensity I_{las} from 10 to $10^5 \mu\text{W}/\mu\text{m}^2$. (c) Steady-state population of the excited state (black solid line, left axis), and the integrated fluorescence intensity (blue dashed line, right axis) as a function of I_{las} for $\lambda_{\text{las}} = 652$ nm. (d) Fluorescence spectra for the laser excitation with varying wavelength λ_{las} from 590 to 652 nm (from low to top curve) and $I_{\text{las}} = 10^4 \mu\text{W}/\mu\text{m}^2$. In all the simulations, we focus on the $S_0 \rightarrow S_2$ excitonic transition with current density along the x -axis, and the STM tip is about $X = 0.6$ nm away from the molecule along the x -axis, and other parameters are same as those in Figure 5.

Furthermore, we investigate with Figure 7d the influence of the laser wavelength λ_{las} on the fluorescence spectrum for given laser intensity $I_{\text{las}} = 10^4 \mu\text{W}/\mu\text{m}^2$. As λ_{las} approaches the molecular resonance at 652 nm, the spectrum intensity increases, and the Mollow side peaks with shorter wavelengths red-shift and finally approach the dominated Mollow peak with longer wavelength. Finally, we emphasize that the laser intensity up to $I_{\text{las}} = 10^4 \mu\text{W}/\mu\text{m}^2$ can be achieved with CW laser, and the much stronger intensity can be realized with the pulsed laser.³⁶ However, at this moment, it is still an open question whether the picocavity can persist in strong laser illumination because of the scarce research on the influence of the laser power on the stability of the picocavity. However, few experimental reports^{1,2} indicated that the picocavity can exist for laser power up to $10^3 \mu\text{W}/\mu\text{m}^2$; thus, it might be possible to sustain the picocavity for slightly larger laser power, like $10^4 \mu\text{W}/\mu\text{m}^2$.

CONCLUSIONS

In conclusion, to address the plasmonic picocavity-controlled fluorescence of a single molecule, as demonstrated in the recent experiment,⁹ we have proposed a semiclassical theory by combining the macroscopic quantum electrodynamics theory and the open quantum system theory. Our simulations not only reproduce the experimental observations but also predict that the molecule can be coherently excited, and the Mollow triplets can be observed in the fluorescence spectrum for sufficiently strong laser illumination, which can be achieved with CW or pulsed laser. Thus, our study highlights the possibility of manipulating coherently the molecular states and exploring the quantum optical phenomena with the plasmonic picocavity.

In the current study, we have relied on the classical electromagnetic simulations, assuming the local response of

electrons and hard boundaries of the metallic nanostructures, to characterize the response of the plasmonic picocavity and its coupling with the molecule. Since the STM junction has a relatively larger gap and the molecule is fairly away from the STM tip in the situations considered, these simulations are expected to produce qualitatively correct results, as justified by the qualitative agreement between the theory and the experiment. However, for the STM junction with much smaller gap or the molecule much closer to the STM tip, other effects, such as the nonlocal response, the spilled-out electron, the Landau damping, and the electron tunneling, might become important and could introduce potentially different phenomena. Indeed, it was observed in the experiment that the molecular fluorescence starts to be suppressed for the STM tip–molecule distance smaller than 0.37 nm; see Figure 3b in ref 9. Thus, in these situations, it would be necessary to go beyond the classical electromagnetic simulations and to adopt the quantum hydrodynamic model^{29,37,38} in combination with the formalism presented in the current study.

ASSOCIATED CONTENT

Supporting Information

The Supporting Information is available free of charge at <https://pubs.acs.org/doi/10.1021/acs.jpcc.2c00531>.

Derivation of effective master equation; far-field spectrum expression; supplemental numerical results: plasmonic response of STM-based nanocavity, extra near-field mapping and Green's function component, molecule-picocavity coupling, formation of mappings based on fluorescence intensity, line-shift and broadening, mappings calculated with the model within dipole approximation (PDF)

AUTHOR INFORMATION

Corresponding Authors

Yuan Zhang – School of Physics and Microelectronics, Zhengzhou University, Zhengzhou 450052, China; orcid.org/0000-0002-8868-1634; Email: yzhuaudipc@zzu.edu.cn

Luxia Wang – Department of Physics, University of Science and Technology Beijing, Beijing 100083, China; Email: luxiaawang@sas.ustb.edu.cn

Authors

Siyuan Lyu – Department of Physics, University of Science and Technology Beijing, Beijing 100083, China

Yao Zhang – Hefei National Laboratory for Physical Sciences at the Microscale and Synergetic Innovation Centre of Quantum Information and Quantum Physics, University of Science and Technology of China, Hefei, Anhui 230026, China

Kainan Chang – GPL, State Key Laboratory of Applied Optics, Changchun Institute of Optics Fine Mechanics and Physics, Chinese Academy of Sciences, Changchun 130033, China

Guangchao Zheng – School of Physics and Microelectronics, Zhengzhou University, Zhengzhou 450052, China; orcid.org/0000-0003-0736-8409

Complete contact information is available at: <https://pubs.acs.org/10.1021/acs.jpcc.2c00531>

Author Contributions

Yuan Zhang devised the theory. Yuan Zhang and S.L. developed the numerical code. Yao Zhang carried out the TDDFT calculation, and S.L. carried out all the other simulations. All the authors contribute to the writing of the manuscript.

Notes

The authors declare no competing financial interest.

ACKNOWLEDGMENTS

We acknowledge project nos. 12004344 and 21902148 from the National Natural Science Foundation of China, joint project no. 21961132023 from the NSFC-DPG. The calculations with Matlab and Gaussian 16 were performed with the supercomputer at the Henan Supercomputer Center.

REFERENCES

- (1) Benz, F.; Schmidt, M. K.; Dreismann, A.; Chikkaraddy, R.; Zhang, Y.; Demetriadou, A.; Carnegie, C.; Ohadi, H.; de Nijs, B.; Esteban, R.; et al. Single-molecule optomechanics in "picocavities". *Science* **2016**, *354*, 726–729.
- (2) Carnegie, C.; Griffiths, J.; de Nijs, B.; Readman, C.; Chikkaraddy, R.; Deacon, W. M.; Zhang, Y.; Szabó, I.; Rosta, E.; Aizpurua, J.; et al. Room-Temperature Optical Picocavities below 1 nm³ Accessing Single-Atom Geometries. *J. Phys. Chem. Lett.* **2018**, *9*, 7146–7151.
- (3) Shin, H.-H.; Yeon, G. J.; Choi, H.-K.; Park, S.-M.; Lee, K. S.; Kim, Z. H. Frequency-Domain Proof of the Existence of Atomic-Scale SERS Hot-Spots. *Nano Lett.* **2018**, *18*, 262–271.
- (4) Zhou, Q.; Lin, S.-P.; Zhang, P.; Chen, X.-W. Quasinormal Mode Analysis of Extremely Localized Optical Field in Body-of-Revolution Plasmonic Structures. *Acta Phys. Sin.* **2019**, *68*, 147104.
- (5) Lee, J.; Tallarida, N.; Chen, X.; Liu, P.; Jensen, L.; Apkarian, V. A. Tip-Enhanced Raman Spectromicroscopy of Co(II)-Tetraphenylporphyrin on Au(111): Toward the Chemists' Microscope. *ACS Nano* **2017**, *11*, 11466–11474.
- (6) Tallarida, N.; Lee, J.; Apkarian, V. A. Tip-Enhanced Raman Spectromicroscopy on the Angstrom Scale: Bare and CO-Terminated Ag Tips. *ACS Nano* **2017**, *11*, 11393–11401.
- (7) Lee, J.; Crampton, K. T.; Tallarida, N.; Apkarian, V. A. Visualizing Vibrational Normal Modes of a Single Molecule with Atomically Confined Light. *Nature* **2019**, *568*, 78–82.
- (8) Doppagne, B.; Neuman, T.; Soria-Martinez, R.; López, L. E. P.; Bulou, H.; Romeo, M.; Berciaud, S.; Scheurer, F.; Aizpurua, J.; Schull, G. Single-Molecule Tautomerization Tracking Through Space- and Time-Resolved Fluorescence Spectroscopy. *Nat. Nanotechnol.* **2020**, *15*, 207–211.
- (9) Yang, B.; Chen, G.; Ghafoor, A.; Zhang, Y.; Zhang, Y.; Zhang, Y.; Luo, Y.; Yang, J.; Sandoghdar, V.; Aizpurua, J.; et al. Sub-Nanometre Resolution in Single-Molecule Photoluminescence Imaging. *Nat. Photonics* **2020**, *14*, 693–699.
- (10) Roslawska, A.; Neuman, T.; Doppagne, B.; Borisov, A. G.; Romeo, M.; Scheurer, F.; Aizpurua, J.; Schull, G. Mapping Lamb, Stark and Purcell Effects at a Chromophore-Picocavity Junction with Hyper-Resolved Fluorescence Microscopy. *arXiv.org (Mesoscale and Nanoscale Physics)*, July 2, 2021. <https://arxiv.org/pdf/2107.01072>.
- (11) He, Z.; Han, Z.; Yuan, J.; Sinyukov, A.; Eleuch, H.; Niu, C.; Zhang, Z.; Lou, J.; Hu, J.; Voronine, D.; et al. Quantum Plasmonic Control of Trions in a Picocavity with Monolayer WS₂. *Sci. Adv.* **2019**, *5*, No. eaau8763.
- (12) Urbietta, M.; Barbry, M.; Zhang, Y.; Koval, P.; Sánchez-Portal, D.; Zabala, N.; Aizpurua, J. Atomic-Scale Lightning Rod Effect in Plasmonic Picocavities: A Classical View to a Quantum Effect. *ACS Nano* **2018**, *12*, 585–595.
- (13) Neuman, T.; Esteban, R.; Casanova, D.; García-Vidal, F. J.; Aizpurua, J. Coupling of Molecular Emitters and Plasmonic Cavities beyond the Point-Dipole Approximation. *Nano Lett.* **2018**, *18*, 2358–2364.
- (14) Zhang, Y.; Dong, Z.-C.; Aizpurua, J. Influence of the Chemical Structure on Molecular Light Emission in Strongly Localized Plasmonic Fields. *J. Phys. Chem. C* **2020**, *124*, 4674–4683.
- (15) Zhang, Y.; Luo, Y.; Zhang, Y.; Yu, Y.-J.; Kuang, Y.-M.; Zhang, L.; Meng, Q.-S.; Luo, Y.; Yang, J.-L.; Dong, Z.-C.; et al. Visualizing coherent intermolecular dipole–dipole coupling in real space. *Nature* **2016**, *531*, 623.
- (16) Zhang, Y.; Meng, Q.-S.; Zhang, L.; Luo, Y.; Yu, Y.-J.; Yang, B.; Zhang, Y.; Esteban, R.; Aizpurua, J.; Luo, Y.; et al. Sub-nanometre control of the coherent interaction between a single molecule and a plasmonic nanocavity. *Nat. Commun.* **2017**, *8*, 15225.
- (17) Luo, Y.; Chen, G.; Zhang, Y.; Zhang, L.; Yu, Y.; Kong, F.; Tian, X.; Zhang, Y.; Shan, C.; Luo, Y.; et al. Electrically Driven Single-Photon Superradiance from Molecular Chains in a Plasmonic Nanocavity. *Phys. Rev. Lett.* **2019**, *122*, 233901.
- (18) Rivera, N.; Kaminer, I. Light–Matter Interactions with Photonic Quasiparticles. *Nat. Rev. Phys.* **2020**, *2*, 538–561.
- (19) Scheel, S.; Buhmann, S. Macroscopic Quantum Electrodynamics-Concepts and Applications. *Acta Phys. Slovaca* **2008**, *58*, 675–809.
- (20) Breuer, H.-P.; Petruccione, F. *The Theory of Open Quantum Systems*; Oxford University Press on Demand, 2002.
- (21) Hohenester, U.; Trügler, A. MNPBEM—A Matlab Toolbox for the Simulation of Plasmonic Nanoparticles. *Comput. Phys. Commun.* **2012**, *183*, 370–381.
- (22) Waxenegger, J.; Trügler, A.; Hohenester, U. Plasmonics Simulations with the MNPBEM Toolbox: Consideration of Substrates and Layer Structures. *Comput. Phys. Commun.* **2015**, *193*, 138–150.
- (23) García de Abajo, F. J. Optical Excitations in Electron Microscopy. *Rev. Mod. Phys.* **2010**, *82*, 209.
- (24) García de Abajo, F. G.; Howie, A. Retarded Field Calculation of Electron Energy Loss in Inhomogeneous Dielectrics. *Phys. Rev. B* **2002**, *65*, 115418.
- (25) Johnson, P. B.; Christy, R.-W. Optical Constants of the Noble Metals. *Phys. Rev. B* **1972**, *6*, 4370.
- (26) Esteban, R.; Zugarramurdi, A.; Zhang, P.; Nordlander, P.; García-Vidal, F. J.; Borisov, A. G.; Aizpurua, J. A classical treatment of

optical tunneling in plasmonic gaps: extending the quantum corrected model to practical situations. *Faraday Discuss.* **2015**, *178*, 151–183.

(27) Esteban, R.; Borisov, A. G.; Nordlander, P.; Aizpurua, J. Bridging quantum and classical plasmonics with a quantum-corrected model. *Nat. Commun.* **2012**, *3*, 825.

(28) Kongsuwan, N.; Demetriadou, A.; Horton, M.; Chikkaraddy, R.; Baumberg, J. J.; Hess, O. Plasmonic Nanocavity Modes: From Near-Field to Far-Field Radiation. *ACS Photonics* **2020**, *7*, 463–471.

(29) Li, W.; Zhou, Q.; Zhang, P.; Chen, X.-W. Bright optical eigenmode of 1 nm³ mode volume. *Phys. Rev. Lett.* **2021**, *126*, 257401.

(30) Zhang, Y.; Esteban, R.; Boto, R. A.; Urbieto, M.; Arrieta, X.; Shan, C.; Li, S.; Baumberg, J. J.; Aizpurua, J. Addressing Molecular Optomechanical Effects in Nanocavity-Enhanced Raman Scattering beyond the Single Plasmonic Mode. *Nanoscale* **2021**, *13*, 1938–1954.

(31) Wu, T.; Yan, W.; Lalanne, P. Bright Plasmons with Cubic Nanometer Mode Volumes through Mode Hybridization. *ACS Photonics* **2021**, *8*, 307–314.

(32) Frisch, M. J.; Trucks, G. W.; Schlegel, H. B.; Scuseria, G. E.; Robb, M. A.; Cheeseman, J. R.; Scalmani, G.; Barone, V.; Mennucci, B.; Petersson, G. A.; Nakatsuji, H.; Caricato, M.; Li, X.; Hratchian, H. P.; Izmaylov, A. F.; Bloino, J.; Zheng, G.; Sonnenberg, J. L.; Hada, M.; Ehara, M.; Toyota, K.; Fukuda, R.; Hasegawa, J.; Ishida, M.; Nakajima, T.; Honda, Y.; Kitao, O.; Nakai, H.; Vreven, T.; Montgomery, J. A., Jr.; Peralta, J. E.; Ogliaro, F.; Bearpark, M.; Heyd, J. J.; Brothers, E.; Kudin, K. N.; Staroverov, V. N.; Kobayashi, R.; Normand, J.; Raghavachari, K.; Rendell, A.; Burant, J. C.; Iyengar, S. S.; Tomasi, J.; Cossi, M.; Rega, N.; Millam, J. M.; Klene, M.; Knox, J. E.; Cross, J. B.; Bakken, V.; Adamo, C.; Jaramillo, J.; Gomperts, R.; Stratmann, R. E.; Yazyev, O.; Austin, A. J.; Cammi, R.; Pomelli, C.; Ochterski, J. W.; Martin, R. L.; Morokuma, K.; Zakrzewski, V. G.; Voth, G. A.; Salvador, P.; Dannenberg, J. J.; Dapprich, S.; Daniels, A. D.; Farkas, O.; Foresman, J. B.; Ortiz, J. V.; Cioslowski, J.; Fox, D. J. *Gaussian 09*, revision A.01; Gaussian, Inc.: Wallingford, CT, 2009.

(33) Duan, S.; Tian, G.; Ji, Y.; Shao, J.; Dong, Z.; Luo, Y. Theoretical Modeling of Plasmon-Enhanced Raman Images of a Single Molecule with Subnanometer Resolution. *J. Am. Chem. Soc.* **2015**, *137*, 9515–9518.

(34) Scully, M. O.; Zubairy, M. S. *Quantum Optics*; Cambridge University Press, 1997.

(35) Ge, R.-C.; Van Vlack, C.; Yao, P.; Young, J. F.; Hughes, S. Accessing Quantum Nanoplasmonics in a Hybrid Quantum Dot-Metal Nanosystem: Mollow Triplet of a Quantum Dot Near a Metal Nanoparticle. *Phys. Rev. B* **2013**, *87*, 205425.

(36) Lombardi, A.; Schmidt, M. K.; Weller, L.; Deacon, W. M.; Benz, F.; De Nijs, B.; Aizpurua, J.; Baumberg, J. J. Pulsed Molecular Optomechanics in Plasmonic Nanocavities: From Nonlinear Vibrational Instabilities to Bond-Breaking. *Phys. Rev. X* **2018**, *8*, 011016.

(37) Ciraci, C. Current-dependent potential for nonlocal absorption in quantum hydrodynamic theory. *Phys. Rev. B* **2017**, *95*, 245434.

(38) Kupresak, M.; Zheng, X.; Vandenbosch, G. A. E.; Moshchalkov, V. V. Comparison of Hydrodynamic Models for the Electromagnetic Nonlocal Response of Nanoparticles. *Adv. Theory Simul.* **2018**, *1*, 1800076.

Recommended by ACS

Fluorescence Brightness, Photostability, and Energy Transfer Enhancement of Immobilized Single Molecules in Zero-Mode Waveguide Nanoapertures

Satyajit Patra, Jérôme Wenger, *et al.*

MAY 11, 2022
ACS PHOTONICS

READ 

Dependence of the Fluorescent Lifetime τ on the Concentration at High Dilution

Heinz Langhals and Thorben Schlücker

AUGUST 10, 2022
THE JOURNAL OF PHYSICAL CHEMISTRY LETTERS

READ 

Visible-Wavelength Multiphoton Activation Confocal Microscopy

Toshiki Kubo, Katsumasa Fujita, *et al.*

AUGUST 30, 2021
ACS PHOTONICS

READ 

Higher-Order Photon Statistics as a New Tool to Reveal Hidden Excited States in a Plasmonic Cavity

Philipp Stegmann, Jianshu Cao, *et al.*

MAY 17, 2022
ACS PHOTONICS

READ 

Get More Suggestions >